

# Magnetic ground state, field-induced transitions, electronic structure, and optical band gap of the frustrated antiferromagnet $\text{GeCo}_2\text{O}_4$

P. Pramanik,<sup>1</sup> S. Ghosh,<sup>1</sup> P. Yanda,<sup>2</sup> D. C. Joshi,<sup>1</sup> S. Pittala,<sup>4</sup> A. Sundaresan,<sup>2</sup> P. K. Mishra,<sup>1</sup> S. Thota,<sup>1,\*</sup> and M. S. Seehra<sup>3,†</sup>

<sup>1</sup>*Department of Physics, Indian Institute of Technology Guwahati, Assam 781039, India*

<sup>2</sup>*School of Advanced Materials and Chemistry and Physics of Materials Unit,*

*Jawaharlal Nehru Centre for Advanced Scientific Research, Bengaluru 560064, India*

<sup>3</sup>*Department of Physics & Astronomy, West Virginia University, Morgantown, West Virginia 26506, USA*

<sup>4</sup>*Department of Physics, Indian Institute of Science, Bangalore-560012, Karnataka, India*



(Received 22 November 2018; revised manuscript received 15 February 2019; published 16 April 2019)

Systematic studies of magnetic ordering, magnetic-field-induced transitions, electronic structure, and optical properties of the frustrated spinel  $\text{GeCo}_2\text{O}_4$  (GCO) are reported. Our results reveal that GCO orders antiferromagnetically (AFM) at  $T_N = 20.4$  K but with significant short-range ferromagnetic (FM) order up to  $T \sim 5 T_N$ . The paramagnetic susceptibility ( $\chi$ ) fits the modified Curie–Weiss law,  $\chi = \chi_0 + C/(T - \theta)$ , with  $\theta = +51$  K for  $100 \text{ K} < T < 800 \text{ K}$ . The fit to high-temperature-series expansion of  $\chi(T)$  yields  $J_1/k_B = 14.7$  K as the dominant FM exchange coupling for the pyrochlore lattice of  $\text{Co}^{2+}$  spins consisting of alternate planes of Kagomé (KGM) and Triangular (TRI) spins lying perpendicular to [111] direction. From the analysis of the  $M$ - $H$  plots at 2 K and published results, three critical fields are identified:  $H_d \sim 11$  kOe due to AFM domains,  $H_{C1} \approx 44$  kOe related to spin-flips and FM ordering of the TRI spins, and  $H_{C2} \approx 97$  kOe related to FM ordering of the KGM spins. For  $H > H_{C2}$ , GCO is a forced ferromagnet with some canting of the spins. Magnetic field dependence of  $T_N$  follows the relation  $T_N(H) = T_N(0) - D_1 H^2$  valid for antiferromagnets with  $D_1 = 6.63 \times 10^{-10} \text{ K/Oe}^2$ . This magnitude of  $T_N(H)$  along with the temperature dependence of  $H_d$ ,  $H_{C1}$ , and  $H_{C2}$  are used to construct the  $H$ - $T$  phase diagram. From the magnitudes of the Curie constant ( $C$ ) and the saturation magnetization at 2 K it is shown that  $\text{Co}^{2+}$  ions in GCO have the ground state with effective spin  $S = 1/2$ . High resolution x-ray photoelectron spectra of  $2p$  and  $3d$  orbitals of Co and Ge confirm the divalent and tetravalent electronic states of Co and Ge, respectively, in GCO. The energy band gap ( $E_g = 3.28$  eV) evaluated using DFT+U calculations is in good agreement with the experimental results ( $E_g = 3.16$  eV) obtained from the diffuse reflectance spectroscopy.

DOI: [10.1103/PhysRevB.99.134422](https://doi.org/10.1103/PhysRevB.99.134422)

## I. INTRODUCTION

Recently, properties of cobalt-based spinels diluted with nonmagnetic metals such as Sn, Ge, Zn, and Ti have received considerable attention, partly because of their excellent electrochemical characteristics useful for high performance batteries in addition to their anomalous low-temperature magnetic ordering [1–11]. Among these spinels, properties and nature of magnetic ordering in  $\text{GeCo}_2\text{O}_4$  (GCO) have received significant attention because it contains pyrochlorelike lattice structure for the magnetic  $\text{Co}^{2+}$  ions, a situation for which magnetic frustration is inherently present as first pointed out by Anderson [12] and elaborated in more recent studies on GCO [7,13–17]. Unlike the inverse ferromagnetic spinels such as  $\text{Co}_2\text{MO}_4$  ( $M = \text{Sn, Ru, Ti}$ ), GCO crystallizes in the normal spinel structure with nonmagnetic  $\text{Ge}^{4+}$  occupying the tetrahedral A-sites and the octahedral B-sites occupied by magnetic  $\text{Co}^{2+}$  ions leading to the structure:  $(\text{Ge}^{4+})_A [2\text{Co}^{2+}]_B\text{O}_4$ . Other B-site magnetic spinels in which considerable amount of magnetic frustration has been reported are  $\text{MgMnO}_3$  [18,19],  $\text{ZnFe}_2\text{O}_4$  [20], and  $\text{AlV}_2\text{O}_4$  [21]. Magnetic properties and nature of magnetic ordering in GCO have been

reported using the data of temperature ( $T$ ) and magnetic-field ( $H$ ) dependence of the magnetization ( $M$ ) [13–15,17,22,23] as well as neutron diffraction techniques [7,14,16,24,25]. These magnetic studies have reported that GCO orders antiferromagnetically (AFM) with a Néel temperature  $T_N$  varying between from 20 K and 23 K although the temperature dependence of paramagnetic susceptibility for  $T > 100$  K when fit to the Curie–Weiss (CW) law;  $\chi = C/(T - \theta)$ , yielded positive  $\theta = 40$ – $80$  K, signifying that the dominant exchange coupling between  $\text{Co}^{2+}$  ions is ferromagnetic (FM). The different magnitudes of  $\theta$  resulted from different temperature range used for fitting the  $\chi$  versus  $T$  data. From the  $M$  versus  $H$  variations measured for  $T < T_N$ , peaks in  $(dM/dH)$  have been reported at  $H_{C1} \approx 44$  kOe and  $H_{C2} \approx 97$  kOe at 4 K [14–16]. However,  $M$  at 2 K is not saturated even in applied  $H$  up to 550 kOe [14]. Several studies in GCO have also reported tetragonal distortion of the cubic lattice accompanying  $T_N$  [15,17,22–25] yielding  $c/a \approx 1.001$  although a recent high-resolution x-ray diffraction study by Barton *et al.* [23] showed that the lattice distortion occurs at  $T_d \approx 16$  K, a few degrees below  $T_N$ , signifying decoupling of the structural distortion and magnetic ordering.

Summarizing the results of neutron diffraction studies in GCO reported by a number of groups [7,14,16,24,25], the following picture of spin ordering in GCO has emerged: the

\*Corresponding author: [subhasht@iitg.ac.in](mailto:subhasht@iitg.ac.in)

†Corresponding author: [Mohindar.Seehra@mail.wvu.edu](mailto:Mohindar.Seehra@mail.wvu.edu)

pyrochlore lattice of  $\text{Co}^{2+}$  ions consist of alternate planes of Kagomé (KGM) spins and spins on triangular (TRI) lattice, all lying in the (111) planes, with the propagation vector  $\vec{k} = (1/2, 1/2, 1/2)$  and with the likely easy direction of  $[11\bar{2}]$ . In applied magnetic field  $H = 0$ , the KGM and TRI spins though parallel within each plane are antiparallel to those in neighboring planes thus yielding an overall AFM ordering. At  $H = H_{C1} \simeq 44$  kOe, any coupling between the KGM and TRI spins breaks down in that TRI spins become ordered ferromagnetically, whereas, the KGM spins in neighboring KGM planes remain AFM ordered. At  $H = H_{C2} \simeq 97$  kOe, the spins in the neighboring KGM planes also become ordered ferromagnetically but with some canting. This canting produces the weak  $H$ -dependence of magnetization for  $H > H_{C2}$ . The magnetic frustration in GCO results from factors such as the geometrical frustration of the pyrochlore lattice of the  $\text{Co}^{2+}$  spins noted earlier along with the presence of several interlayer antiferromagnetic exchange couplings among the KGM and TRI spins [16,24–26], in addition to the dominant in-plane ferromagnetic exchange coupling.

The above summary of the important results reported in literature shows that some important issues regarding the nature of magnetism in GCO are still not settled. For example, a proper interpretation of the temperature dependence of the paramagnetic susceptibility in terms of the CW law or more elaborate models and its correlation with the measured values of the magnetization for  $T < T_N$  has not been made. Also, results of the magnetic studies need to be reconciled with those from the recent electron magnetic resonance (EMR) studies in single crystals of GCO by Okubo *et al.* [27] who reported the observation of a broad EMR line at 86 K with the  $g$  value = 5.26 for  $H$  along [111] with similar  $g$  values along the [100] and [110] directions. The line broadens out at higher  $T$  because of rapid spin-lattice relaxation and for  $T < T_N$ , the observed AFMR (antiferromagnetic resonance) lines are yet to be interpreted quantitatively. The above issues are important regarding the nature of the ground state of  $\text{Co}^{2+}$  in GCO. As noted for  $\text{CoCl}_2$  [28],  $\beta - \text{Co}(\text{OH})_2$  [29] and more recently by Tomiyasu *et al.* [25,26] in GCO,  $\text{Co}^{2+}$  ions in octahedral crystalline field with small trigonal distortion combined with the effects of spin-orbit coupling  $\lambda \vec{L} \cdot \vec{S}$  ( $\lambda = -180 \text{ cm}^{-1}$ ) leads to Kramer doublet as the ground state with effective spin  $S = 1/2$ . This doublet is separated from the nearby levels with effective  $S = 3/2$  situated at  $\sim 450$  K and effective  $S = 5/2$  at  $\sim 1000$  K. Neutron diffraction measurements in GCO by Diaz *et al.* [13,14] reported  $3.02 \mu_B$  as the magnetic moment on  $\text{Co}^{2+}$  ion at 1.5 K and about  $6.3 \mu_B/\text{f.u.}$  as the saturation magnetization. These observations of the magnetization data in GCO for  $T > T_N$  need to be reconciled with the magnetization data for  $T < T_N$  for a proper understanding of the nature of magnetism in this system. Finally, building on the results of Hoshi *et al.* [15],  $H$ - $T$  phase diagram for GCO needs to be established and magnitudes of the dominant exchange couplings need to be determined.

In this paper, we report results and analyses from our detailed investigation of the temperature and magnetic field dependence of the magnetization of a polycrystalline sample of GCO to address the above questions. XPS (x-ray photoelectron spectroscopy) combined with the Rietveld analysis

of the x-ray diffraction patterns is used to show that  $\text{Ge}^{4+}$  indeed occupies the tetrahedral A-site whereas the electron states of cobalt occupying the B-sites is  $\text{Co}^{2+}$ . Temperature dependence of paramagnetic susceptibility above  $T_N = 20.4$  K is analyzed with the modified Curie-Weiss law including temperature-independent contribution and it is shown that neglecting the temperature independent contribution to the paramagnetic susceptibility has significant effect on the derived parameters. The magnitude of the dominant ferromagnetic exchange coupling is determined from the fit of paramagnetic susceptibility to high temperature series and significant amount of short-range magnetic order at  $T$  up to  $\sim 5T_N$  is evident from this analysis. We also show that the ground state with effective spin  $S = 1/2$  of  $\text{Co}^{2+}$  ions can systematically explain the measured magnetization both above and below  $T_N$  and magnetic moment of  $\text{Co}^{2+}$  ions measured by neutron diffraction experiments. A new  $H$ - $T$  phase diagram for GCO is presented based on the temperature dependence of three critical fields and magnetic field dependence of  $T_N$ . New results from optical absorption studies in GCO show that its energy band gap  $E_g \simeq 3.16$  eV, in agreement with  $E_g = 3.28$  eV obtained from our DFT+U calculations included here. Detailed of these results along with their discussion and analysis are given in the following pages.

## II. EXPERIMENTAL DETAILS

The polycrystalline sample of  $\text{GeCo}_2\text{O}_4$  (GCO) with bulk-size grains was synthesized by the standard solid-state reaction route using the following procedure: Stoichiometric amounts of  $\text{Co}_3\text{O}_4$  and  $\text{GeO}_2$  were mixed in an agate mortar and sintered in air at  $1000^\circ\text{C}$ . After the intermediate re-grinding and pelletizing process, the sample was sintered at  $1200^\circ\text{C}$  for 12 h in air using a high-temperature tube furnace from Nabertherm (Germany), followed by natural cooling to room temperature. The structural characterization of the sample was done using a high-resolution XPERT-PRO diffractometer (Co- $K_\alpha$  radiation with  $\lambda = 1.78901 \text{ \AA}$ ). The Rietveld refinement of the diffraction data was performed using the FullProf program. Magnetization measurements were done using a SQUID-based magnetometer MPMS from Quantum Design. For optical characterization we used spectrophotometer (Perkin Elmer Lambda-950) with diffuse reflectance accessory (DRA) covering the wavelength range of 200–800 nm. For determining the electronic states of the ions and elemental analysis, we used a high-resolution x-ray photoelectron spectroscope from Kratos Axis Ultra, Model AXIS 165 equipped with an ion-gun (EX-05) for cleaning the surface. The binding-energy resolution is 0.01 eV, while background correction was done by using the Tougaard algorithm and data were fitted using the x-ray photoelectron spectroscopy software XPSFIT 4.1. The core-level binding energies were aligned with the carbon binding energy of 284.8 eV.

## III. ELECTRONIC AND STRUCTURAL CHARACTERIZATION

### A. X-ray photoelectron spectroscopy (XPS)

Figure 1 shows photoelectron intensity (I) versus binding-energy (eV) spectra of GCO for the individual elements:

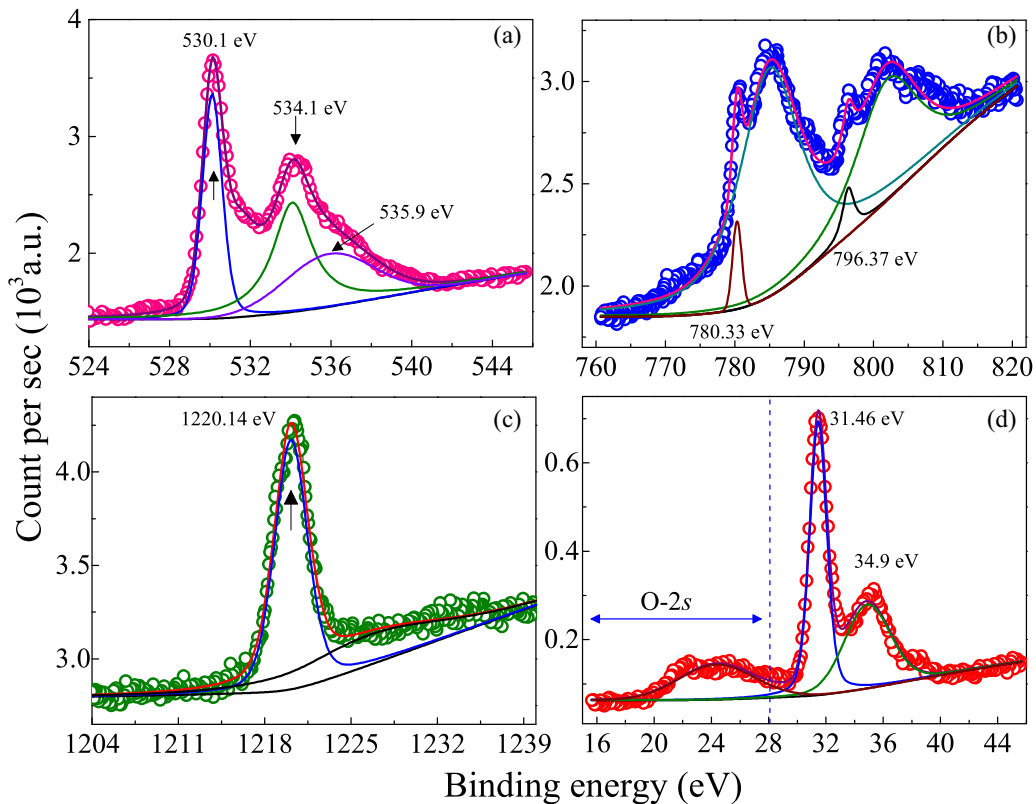


FIG. 1. X-ray-photoemission spectra of (a) O-1s, (b) Co-2p, and (c, d) Ge-2p<sub>3/2</sub> and Ge-3d peaks in the GeCo<sub>2</sub>O<sub>4</sub> sample.

(i) O-1s, (ii) Co-2p, (iii) Ge-2p<sub>3/2</sub>, and (iv) Ge-3d<sub>5/2</sub> core-level photoelectrons. All these spectra were calibrated by selecting the binding energy of carbon C-1s orbital (located at  $E_C = 284.8$  eV) as an internal reference. The O-1s spectrum is resolved into three Gaussian-Lorentzian peaks centered at 530.1, 534.1, and 535.9 eV [as shown by arrow marks in Fig. 1(a)] [30–32]. The origin of the most intense peak at 530.1 eV is associated with the bonding between metal and lattice oxygen, in the present case it is Ge-O and Co-O [31,32]. While the second-highest intense peak appears at 534.1 eV, which is associated with the surface-absorbed oxygen [32]. The additional broad peak at 535.9 eV is mainly associated with the excess oxygen present in the system [32]. The asymmetric behavior observed in O-1s core-level spectrum is mainly due to the presence of oxygen vacancies and different atomic environment faced by the O<sup>2-</sup> anions at the Wyckoff positions 32e (0.2378, 0.2378, 0.2378) [30,32]. The Co-2p core-level XPS spectrum is deconvoluted into two major peaks and two broad satellite peaks centered at 780.33 eV (Co-2p<sub>3/2</sub>), 796.37 eV (Co-2p<sub>1/2</sub>) and 785.03 eV, 802.01 eV, respectively (the full width of half maximum, FWHM  $\sim 10$  eV for the satellite peak). The binding energy separation between the doublet  $\Delta E_{\text{Co}}(2p_{1/2} - 2p_{3/2})$  is 16.04 eV signifying the divalent oxidation state of octahedrally coordinated “Co” inside the GeCo<sub>2</sub>O<sub>4</sub> [33,34]. It is notable that the higher intensities of satellite peaks as compared to the doublets characterize the loss in the system. The electronic state of Ge was analyzed by considering only the Ge-2p<sub>3/2</sub> core-level region, since Ge-2p exhibits significantly high spin-orbit splitting  $\Delta E_{\text{Ge}}(2p_{1/2} - 2p_{3/2}) \sim 31.1$  eV [35–38]. Figure 1(c) shows the Ge-2p<sub>3/2</sub> core-level photoelectron spectrum. This

spectrum comprises a main peak and a satellite peak centered at 1220.14 and 1226.56 eV, respectively, suggesting the presence of tetravalent oxidation state of Ge [36–38]. To further confirm this, we have analyzed the high-energy Ge-3d x-ray photoelectron spectrum shown in Fig. 1(d). Here, the peak profile of Ge-3d is resolved into two peaks located at 31.46 and 34.89 eV associated with the binding energies of Ge<sup>0+</sup> (Ge-3d) and Ge<sup>4+</sup>, respectively, and the binding energy separation  $\Delta \sim 3.43$  eV confirming the tetravalent oxidation state of germanium ion. An additional photoelectron peak was observed at 24.35 eV, which is originating due to the emission of O-2s core-level photoelectrons [39]. For determining the exact location (either tetrahedral-A or octahedral-B sites) of the cations and site occupancies we performed a detailed crystal structure study presented below [37,38].

## B. Structural characterization

Figure 2 shows the x-ray diffraction (XRD) patterns recorded at room temperature for the GCO sample along with the corresponding Rietveld refinement data. The spectra confirm the cubic spinel structure of GCO (space group  $Fd\bar{3}m$ ) without evidence of any impurity phase. The Rietveld refinement was done by considering two cases: Ge<sup>4+</sup> occupying the (a) tetrahedral A-sites and (b) octahedral B-sites. The red hollow symbols shown in Fig. 2 represent the experimental data, and the black solid lines are the simulated XRD patterns. The blue line is the difference between the experimental and simulated patterns with the vertical straight lines representing the position of the Bragg peaks. The goodness of the fit ( $\sigma$ ) of the Rietveld refinement is 2.8 when Ge<sup>4+</sup> occupies the

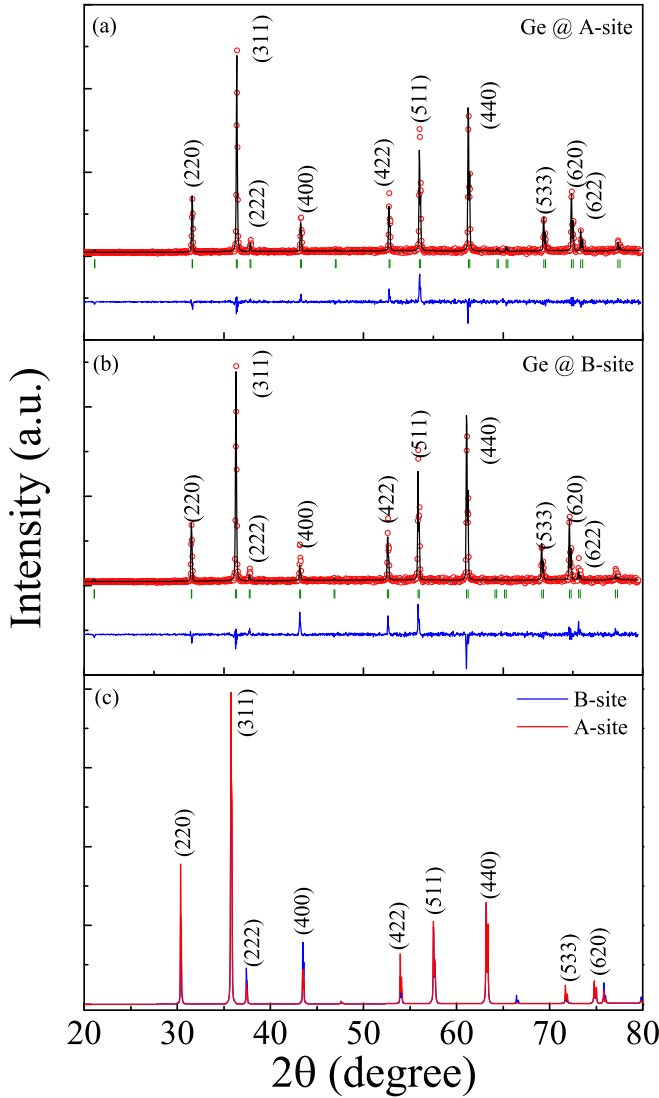


FIG. 2. Room temperature x-ray diffraction data of  $\text{GeCo}_2\text{O}_4$  along with its Rietveld refinement patterns: (a) Ge-placed at tetrahedral-A site and (b) Ge at the octahedral B-site. Panel (c) shows the simulated x-ray diffraction (XRD) patterns with the red color pattern for Ge located at tetrahedral-A site and blue color pattern for Ge-situated at octahedral B-site.

tetrahedral A-site and  $\sigma \sim 6.8$  when it resides in the octahedral B-site, indicating that  $\text{Ge}^{4+}$  occupies the tetrahedral A-site (normal spinel) instead of B-site (inverse spinel) in GCO. This is different from  $\text{SnCo}_2\text{O}_4$  and  $\text{TiCo}_2\text{O}_4$  which exhibit inverse spinel structure in that the nonmagnetic elements Sn and Ti occupy the B sites. The Wyckoff positions for  $\text{O}^{2-}$ ,  $\text{Co}^{2+}$ , and  $\text{Ge}^{4+}$  are  $32e(0.2378, 0.2378, 0.2378)$ ,  $16c(0, 0, 0)$ , and  $8b(3/8, 3/8, 3/8)$ , respectively, if GCO crystallizes in normal spinel structure. However, if  $\text{GeCo}_2\text{O}_4$  crystallizes in inverse spinel structure, then two  $\text{Co}^{2+}$  Wyckoff positions locate at (i)  $16c(0, 0, 0)$  and (ii)  $8b(3/8, 3/8, 3/8)$ ; and  $\text{Ge}^{4+}$  occupies the Wyckoff position  $16c(0, 0, 0)$ . Considering these two different site occupancies we have simulated the XRD patterns for  $\text{GeCo}_2\text{O}_4$ , Fig. 2(c), where the pattern generated for the normal (inverse) spinel configuration is shown in red (blue) solid line. From these simulated patterns it is noted that if

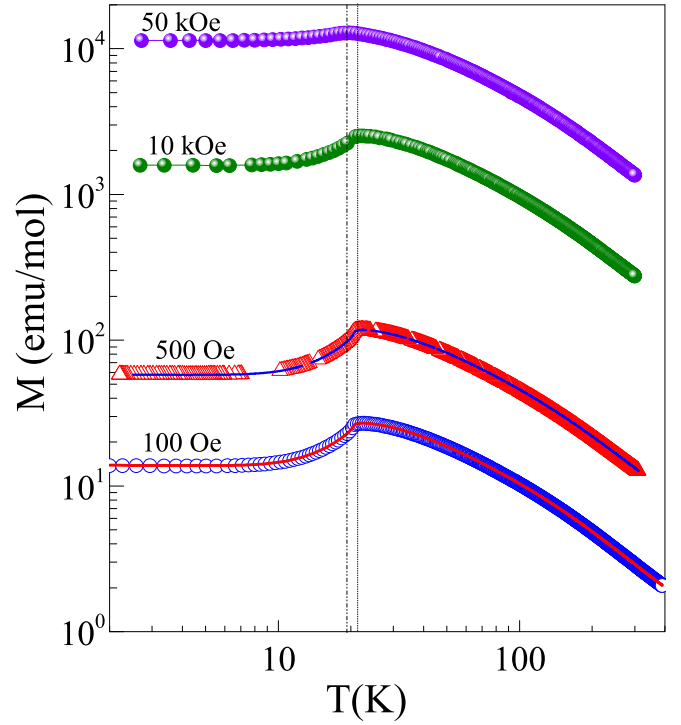


FIG. 3. Temperature dependence of magnetization,  $M(T)$ , of  $\text{GeCo}_2\text{O}_4$  measured with different applied DC-magnetic fields under the zero-field-cooled (symbols) and field-cooled (solid lines) conditions. Log scale is used for temperatures to highlight the data at the lower temperatures.

$\text{Ge}^{4+}$  occupies the octahedral B-sites, then peak intensities of the (222) and (400) lines should be higher as compared to the  $\text{Ge}^{4+}$  located at A-sites. It is noted that our experimental data of intensities match well with the simulated pattern generated for  $8b$  Wyckoff position (A-site) occupied by  $\text{Ge}^{4+}$  ions. Hence, these comparisons rule out the possibility of  $\text{Ge}^{4+}$  occupying the octahedral B-sites in GCO, which is usually observed in its sister compounds of  $\text{SnCo}_2\text{O}_4$ ,  $\text{TiCo}_2\text{O}_4$ , and  $\text{RuCo}_2\text{O}_4$  [40]. In addition, from the Rietveld refinement we have evaluated the bond-angle Co-O-Co ( $81.1^\circ$ ) and bond-length Co-O ( $2.96 \text{ \AA}$ ), which are consistent with our density functional theory calculations ( $89.7^\circ$  and  $2.12 \text{ \AA}$ ) presented later (Sec. V).

## IV. MAGNETIC PROPERTIES

### A. Temperature dependence of magnetic susceptibility

Temperature dependence of the magnetization ( $M$ ) measured in the temperature range of 2 K to 400 K in applied  $H = 100 \text{ Oe}$ ,  $500 \text{ Oe}$ ,  $10 \text{ kOe}$ , and  $50 \text{ kOe}$ , under the zero-field-cooled (ZFC) and field-cooled (FC) protocols is plotted in Fig. 3. The peaks in  $M$  near 20 K are associated with the Néel temperature  $T_N$ ; more accurate determination of  $T_N$  and its  $H$  dependence is presented later. To analyze the temperature dependence of  $\chi = M/H$  we have incorporated the data of Diaz *et al.* [13] for  $T$  up to 800 K and these combined data of  $\chi$  versus  $T$  are shown in Fig. 4(a). We first analyzed these data of  $\chi$  versus  $T$  in terms of Curie-law given by  $\chi = C/T$  with

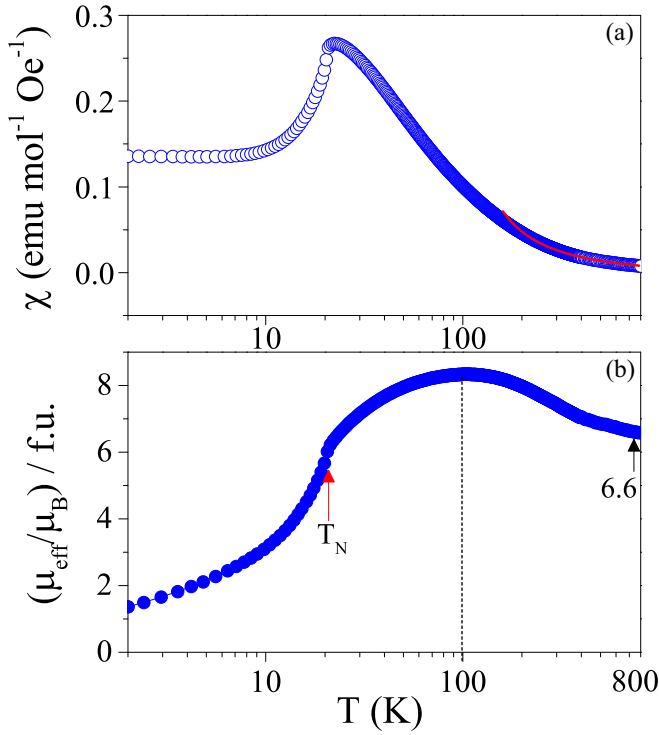


FIG. 4. (a) Temperature variation of magnetic susceptibility,  $\chi(T)$ , measured for  $H_{DC} = 100$  Oe. Log scale for temperature scale is used to show details of the low-temperature variations. (b) Temperature variation of the ratio of effective magnetic moment  $\mu_{\text{eff}}$  and Bohr magneton  $\mu_B$  determined using the Curie law.

$C = N_A \mu^2 / 3k_B$  ( $N_A =$  Avogadro's number,  $\mu =$  magnetic moment,  $k_B =$  Boltzmann constant). Note that the measured  $M$  and  $\chi$  in units of emu/g is multiplied by the molecular weight of GCO (M.W. = 254.50 mol/g) to obtain  $M$  and  $\chi$  in molar units. From the Curie-law, effective  $(\mu/\mu_B)^2 = 3k_B \chi T / N_A \mu_B^2$  can be determined. Following analysis for  $\beta$ -Co(OH)<sub>2</sub> [29], the plot of  $(\mu/\mu_B)$  per formula unit (f.u.) of GCO against temperature depicted in Fig. 3(b) shows that with decrease in temperature,  $(\mu/\mu_B)$  increases peaking near 100 K and then decreases. If there were no exchange coupling among  $\text{Co}^{2+}$  ions, then  $(\mu/\mu_B)$  should be temperature independent. The increase in  $(\mu/\mu_B)$  from 800 to 100 K shows ferromagnetic (FM) coupling, whereas decrease of  $(\mu/\mu_B)$  for  $T < 100$  K is indicative of onset of antiferromagnetic (AFM) coupling. The inflexion in the  $(\mu/\mu_B)$  versus  $T$  curve near 20 K is due to  $T_N$ . It is noted that the peak in  $(\mu/\mu_B)$  near 100 K in Fig. 4(b) is like the broad peak near 100 K in  $C_P/T$  versus  $T$  data of Lashley *et al.* [22] and it represents considerable amount of short-range FM ordering up to  $5T_N$ .

The data of  $\chi$  versus  $T$  for  $T > T_N$  is often done using the modified Curie-Weiss (CW) law given by

$$\chi = \chi_0 + C/(T - \theta). \quad (1)$$

Here  $\chi_0$  represents contributions from diamagnetic susceptibility which is present in all materials and Van Vleck susceptibility if applicable [41]. Although magnitude of  $\chi_0$  may be comparatively negligible for low temperatures, its inclusion in the high temperature data can be quite important for accurate

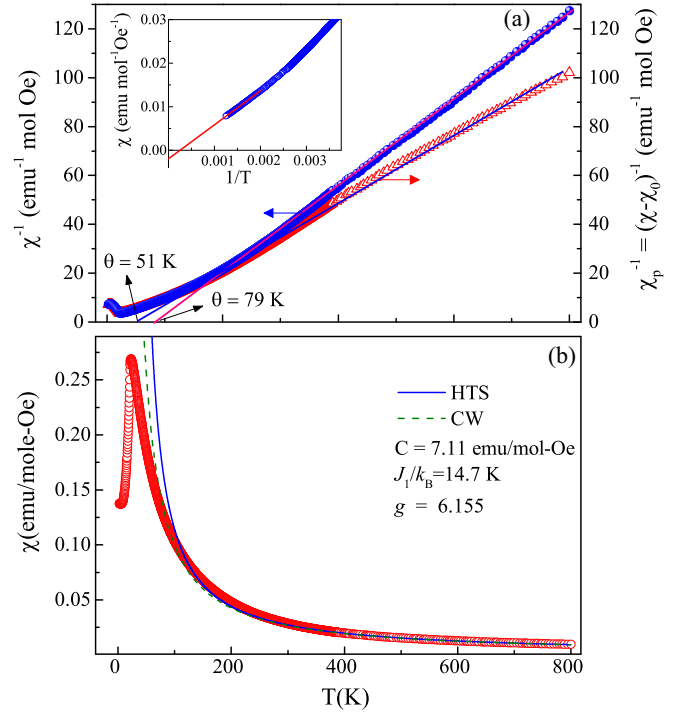


FIG. 5. (a) Inset shows the plot of magnetic susceptibility  $\chi$  ( $H = 100$  Oe) of  $\text{GeCo}_2\text{O}_4$  vs. inverse temperature to determine temperature independent term  $\chi_0 = -1.95 \times 10^{-3}$  emu mol<sup>-1</sup> Oe<sup>-1</sup> from the y intercept. Other plots are temperature variations of  $\chi_p^{-1} (= \chi - \chi_0)^{-1}$  after correcting for  $\chi_0$  and that of  $\chi^{-1}(T)$  without correcting for  $\chi_0$  with the solid lines as fits to the Curie-Weiss law. (b) Temperature variation of magnetic susceptibility with the solid line as fit to the high temperature series (HTS) expression [Eq. (2)] and the dashed line as fit to the Curie-Weiss law [Eq. (1)].

determination of the parameters  $C$  and  $\theta$ . To experimentally determine  $\chi_0$ , the data of  $\chi$  versus  $(1/T)$  is plotted in the inset of Fig. 5(a) and  $\chi_0 = \chi$  in the limit of  $1/T \rightarrow 0$  where the contribution of  $C/(T - \theta)$  should go to zero. This analysis yields  $\chi_0 = -1.95 \times 10^{-3}$  emu mol<sup>-1</sup> Oe<sup>-1</sup>. Using this, the plot of  $1/\chi_P = 1/(\chi - \chi_0)$  versus  $T$  is made to determine  $C$  and  $\theta$ . In Fig. 5(a), we show the plots of  $\chi_P^{-1}$  versus  $T$  and  $\chi^{-1}$  versus  $T$ . The plot of  $\chi_P^{-1}$  versus  $T$  yields a straight line for  $T > 100$  K yielding  $\theta = 51$  K, whereas  $\chi^{-1}$  versus  $T$  plot yields a straight line for  $T > 170$  K with  $\theta = 79$  K. The magnitudes of  $\theta$ ,  $C$  and calculated  $(\mu/\mu_B)$  from  $C$  and other derived quantities are listed in Table I. This analysis shows that the magnitudes of  $\theta$  and  $C$  are affected by  $\chi_0$ . Since  $\chi_0$  was ignored in all previous publications on GCO, the magnitudes of  $C$  and  $(\mu/\mu_B)$  determined here are somewhat different and in our view more accurate.

The above analysis yields  $C/\text{f.u.} = N_A \mu^2 / 3k_B$ . Since  $C$  is proportional to  $\mu^2$  and GCO contains two  $\text{Co}^{2+}$  ions/f.u., then  $\mu^2/\text{f.u.} = \mu_1^2 + \mu_2^2$ , where  $\mu_1 = \mu_2 = \mu(\text{Co}^{2+})$  in this case. So  $\mu/\text{Co}^{2+} = (\mu/\text{f.u.})/\sqrt{2}$ . This distinction has also not been stressed in other publications. In Table I, we have listed the magnitudes of  $C$ ,  $\theta$  and other derived parameters based on both the  $\chi_P^{-1}$  versus  $T$  and  $\chi^{-1}$  versus  $T$  fits. Using  $\mu^2 = g^2 S(S + 1)$ , the magnitudes of derived  $g$  for both  $S = 3/2$  and effective  $S = 1/2$  are also listed along with

TABLE I. Parameters obtained from the Curie-Weiss fitting of magnetic susceptibility versus temperature data.

| Parameters                           | $\chi_P^{-1}$ vs. $T$ fit     | $\chi^{-1}$ vs. $T$ fit       |
|--------------------------------------|-------------------------------|-------------------------------|
| $C$ (emu/mol K)                      | $7.11 \pm 0.04$               | $5.78 \pm 0.03$               |
| $\theta$ (K)                         | 51                            | 79                            |
| $\mu/f.u.$                           | $7.538 \mu_B \pm 0.023 \mu_B$ | $6.796 \mu_B \pm 0.014 \mu_B$ |
| $\mu/Co^{2+}$                        | $5.330 \mu_B \pm 0.016 \mu_B$ | $4.80 \mu_B \pm 0.01 \mu_B$   |
| $g/Co^{2+}$ for $S = 3/2$            | $2.758 \pm 0.002$             | $2.483 \pm 0.004$             |
| $g/Co^{2+}$ for $S = 1/2$            | $6.1546 \pm 0.019$            | $5.548 \pm 0.012$             |
| $\mu_z = gS/Co^{2+}$ , for $S = 3/2$ | $4.13 \mu_B$                  | $3.72 \mu_B$                  |
| $\mu_z = gS/Co^{2+}$ , for $S = 1/2$ | $3.077 \mu_B$                 | $2.776 \mu_B$                 |
| $M_S = 2N_A gS$ for $S = 3/2$        | 46,208 emu/mol                | 41,550 emu/mol                |
| $M_S = 2N_A gS$ for $S = 1/2$        | 34,372 emu/mol                | 31,002 emu/mol                |

the magnetic moment  $\mu_z = gS$ . Later, these magnitudes are compared with experimental parameters.

### B. Paramagnetic susceptibility, high temperature series, and exchange constant

We next fit the data of  $\chi_P$  versus  $T$  to the high temperature series (HTS) of a spin  $S = 1/2$  Heisenberg system for a pyrochlore lattice which is valid for GCO. This HTS is written as [42,43]

$$\chi_P = \frac{C}{T} \sum_{n=0}^{\infty} C_n \left( \frac{-2J_1}{k_B T} \right)^n. \quad (2)$$

Using the information given in Ref. [42], we determined  $C_0 = 1$ ,  $C_1 = 3/2$ ,  $C_2 = 3/2$ ,  $C_3 = -1.0625$ ,  $C_4 = 0.664062$ ,  $C_5 = -0.60624$ ,  $C_6 = 0.65778$ ,  $C_7 = -0.49058$ , and  $C_8 = 0.187472$ . Here  $J_1$  is the exchange interaction in the Heisenberg exchange Hamiltonian  $-2J_1 \vec{S}_1 \cdot \vec{S}_2$  so that a positive  $J_1$  represents ferromagnetic coupling. The first two terms of series of Eq. (2) can be written in the CW form with  $\theta = 3J_1/k_B$ . Using  $\theta = 51$  K yields  $J_1/k_B = 17$  K as the dominant ferromagnetic interaction. Using all eight terms in the series and  $C = 7.11$  emu K/mol Oe and  $g = 6.155$  listed in Table I yields a pretty decent fit to the  $\chi_P$  versus  $T$  data in the 100 to 800 K range [see Fig. 5(b)]. The fit to the CW law is also shown in Fig. 5(b). The fit to HTS is only a slight improvement over the fit to the CW law with  $J_1/k_B = 14.7$  K determined from HTS compared to  $J_1/k_B = 17$  K evaluated from the CW fit. The fit of the data to HTS for  $T < 100$  K is poor because of the onset of the weaker AFM exchange coupling in this range as noted earlier. Since HTS for more than one exchange constant is not available, no information on the AFM exchange constants can be determined from this analysis.

### C. Saturation magnetization and magnetic ground state

As noted in the Introduction, the ground state of  $Co^{2+}$  ions in GCO is expected to have an effective spin  $S = 1/2$ . So, the low-temperature experimental results of saturation magnetization and magnetic moment per  $Co^{2+}$  ion should be interpreted on that basis. Neutron diffraction measurements in GCO by Diaz *et al.* [13,14] reported  $3.02 \mu_B$  as the magnetic moment on  $Co^{2+}$  at 1.5 K and about  $6.3 \mu_B/f.u.$  as the saturation magnetization. The magnitude of  $6.3 \mu_B/f.u.$

as the saturation magnetization  $M_S$  leads to  $M_S = 35,184$  emu/mol which is in excellent agreement with the calculated  $M_S = 34,372$  emu/mol using  $S = 1/2$  as the ground state. Considering  $S = 3/2$  as the ground state would yield the calculated  $M_S = 46,208$  emu/mol which is over 30% larger than the measured value  $M_S = 35,184$  emu/mol. Using  $g = 6.1546$  determined for  $S = 1/2$  from the Curie constant  $C$  (see Table I),  $\mu_z = gS = 3.077 \mu_B$  per  $Co^{2+}$  ion is determined in good agreement with the experimental results of Diaz *et al.* [14]. One may question the magnitude of  $g = 6.1546$  derived for the  $S = 1/2$  state using the fit to the CW law. However,  $g$  values up to 6.6 have been reported for  $Co^{2+}$  ions [29,44]. Also, EMR measurements reported by Okubo *et al.* [27] in GCO reported a broad line for  $T > T_N$  with  $g = 5.26$  for  $H$  along [111] as noted in the Introduction. Lashley *et al.* [22] in their fitting of  $\chi^{-1}$  versus  $T$  data above  $T_N$  without including the exchange interaction determined  $g = 6.6$  for the ground state. These considerations of the measured magnetic moment and magnetization for  $T \ll T_N$  and their agreement with the calculated values assuming  $S = 1/2$  as the ground state show that the magnetization data above  $T_N$  and below  $T_N$  in GCO can be reconciled with a single set of parameters. We consider this to be an important contribution of this work.

### D. Néel temperature and its magnetic field dependence:

In Fig. 4, the temperature dependence of the  $\chi(FC)$  measured in  $H = 100$  Oe, 500 Oe, 10 kOe, and 50 kOe showed a peak in  $\chi(FC)$  near  $T_P \simeq 22$  K with slight decrease in  $T_P$  with increase in  $H$ . Although  $T_P$  is often associated with onset of AFM ordering, the position of the Néel temperature  $T_N$  in antiferromagnets is more accurately determined by the peak in  $\partial(\chi T)/\partial T$  since  $\chi T$  represents the magnetic energy and so specific heat  $C_p \propto \partial(\chi T)/\partial T$  [45]. In Fig. 6, the plot of  $\partial(\chi T)/\partial T$  versus  $T$  is shown giving  $T_N = 20.4$  K, 20.3 K, 20.0 K, and 18.0 K for  $H = 100$  Oe, 500 Oe, 10 kOe, and 50 kOe, respectively. Our observed  $T_N = 20.4$  K for  $H = 100$  Oe is in good agreement with  $T_N = 20.6$  K reported by Lashley *et al.* [22], the peak position in the specific heat in zero applied field. Lashley *et al.* [22] also reported the shift in the peak position of the  $C_p$  versus  $T$  data in applied fields up to  $H = 140$  kOe. The variation of  $T_N$  versus  $H$  is fitted to the molecular-field-based

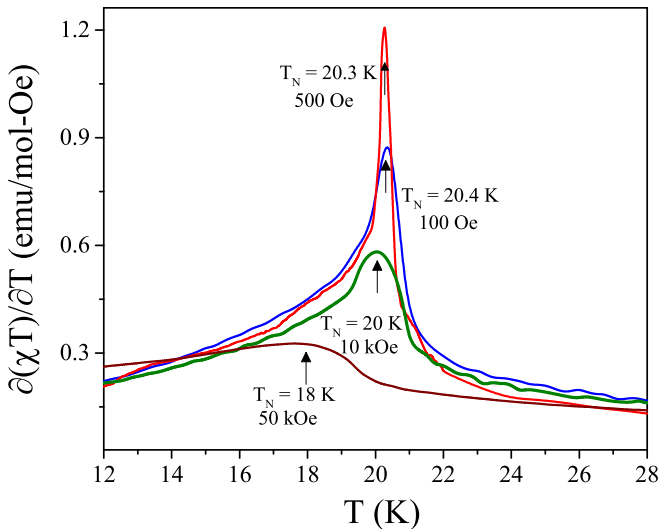


FIG. 6. Temperature derivative of the product of magnetic susceptibility  $\chi$  and temperature  $T$  of the  $\text{GeCo}_2\text{O}_4$  sample is plotted as a function of temperature for different applied DC-magnetic fields. The peaks marked by arrows define the Néel temperature  $T_N$ .

theoretical equation [46,47]

$$T_N(H) = T_N(0) - D_1 H^2, \quad (3)$$

$$D_1 = g^2 \mu_B^2 (2S^2 + 2S + 1) / 40k_B^2 T_N(0).$$

The plot of  $T_N$  versus  $H^2$  is shown in Fig. 7 in which we have also included the data reported by Lashley *et al.* [22]. The expected linear variation is observed with  $D_1 = 6.6 \times 10^{-10} \text{ K/Oe}^2$ . Using  $g=6.1546$  and  $S = 1/2$  determined earlier for GCO (Table I) yields  $D_1 = 5.24 \times 10^{-10} \text{ K/Oe}^2$ , in fair agreement with the experimental  $D_1 = 6.6 \times 10^{-10} \text{ K/Oe}^2$ . A similar discrepancy between the

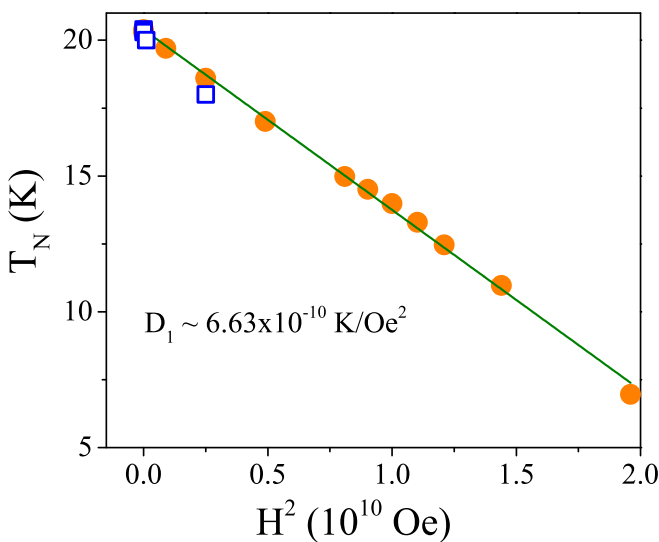


FIG. 7. Variation of the Néel temperatures  $T_N$  versus  $H^2$  of GCO plotted to test the equation  $T_N(H) = T_N(0) - D_1 H^2$ . The solid line is the linear fit to the experimental data points obtained from  $C_P(T)$  vs.  $T$  data of Lashley *et al.* [22] (solid circles) and from the present work of  $d(\chi T)/dT$  vs.  $T$  data of Fig. 6 (open squares).

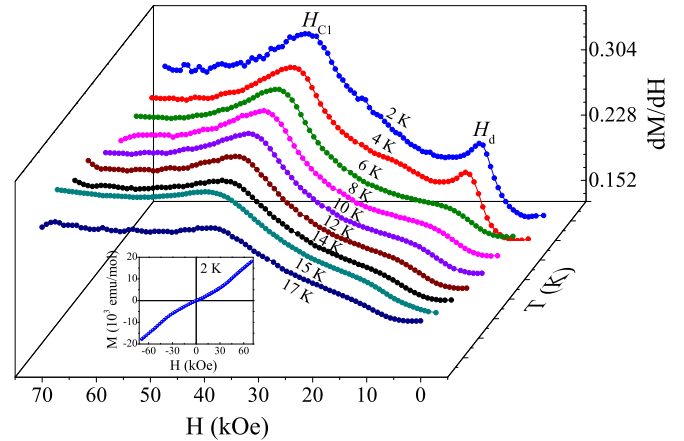


FIG. 8. Plots of computed  $dM/dH$  versus  $H$  for  $\text{GeCo}_2\text{O}_4$  determined from the data of isothermal magnetization curves at different temperatures such as the curve shown in the inset measured at 2 K. The positions of the peaks determine the critical fields  $H_{C1}$  and  $H_d$  used in the  $H$ - $T$  phase diagram of Fig. 9.

experimental and measured  $D_1$  has been reported in antiferromagnets  $\text{MnF}_2$  [47] and  $\text{Er}_2\text{O}_3$  [46], and it has been attributed to the molecular field approximation used in driving Eq. (3). Using  $D_1 = 6.6 \times 10^{-10} \text{ K/Oe}^2$  yields  $H_C = 176 \text{ kOe}$  as the magnetic field for which  $T_N(H) \rightarrow 0 \text{ K}$ . This information on  $H_C$  is used in the following section.

### E. Magnetic-field-induced transitions and $H$ - $T$ phase diagram

The variation of  $M$  with  $H$  up to 70 kOe recorded at 2 K is shown in the inset of Fig. 8. From such isotherms of  $M$  versus  $H$  data at different temperatures,  $dM/dH$  versus  $H$  was computed and these plots are shown in Fig. 8. From the peak positions in  $dM/dH$ , two transitions are evident, one at  $H_d \simeq 11 \text{ kOe}$  and the other at  $H_{C1} \simeq 44 \text{ kOe}$ . Temperature dependence of  $H_d$  and  $H_{C1}$  are displayed in Fig. 9, from which it is evident that the intensity of the peak showing  $H_d$  weakens rapidly with increasing temperature, whereas the peak corresponding to  $H_{C1}$  eventually shifts to lower  $H$  on approach to  $T_N \simeq 20.4 \text{ K}$ . Several other groups [13,14,24] have also reported  $M$  versus  $H$  data in GCO for  $T \ll T_N$  for  $H$  up to 550 kOe and have shown the transition at  $H_{C1} \simeq 44 \text{ kOe}$  and  $H_{C2} \simeq 97 \text{ kOe}$ . Since our measurements are limited to  $H$  up to 70 kOe, we did not observe  $H_{C2} \simeq 97 \text{ kOe}$ . The recent measurements of Fabr eges *et al.* [24] who employed neutron and x-ray diffraction in single crystals of GCO are particularly noteworthy in understanding the nature of the  $H$ -induced phase transitions in  $H$  up to 100 kOe. Fabr eges *et al.* [24] also reported a broad transition near  $H_d \simeq 15 \text{ kOe}$  which they associated with domain reorientation in addition to the transitions at  $H_{C1}$  and  $H_{C2}$ . Below we summarize the nature of three transitions at  $H_d$ ,  $H_{C1}$ , and  $H_{C2}$  and present  $H$ - $T$  phase diagram for GCO, not reported before.

In the pyrochlore structure of  $\text{Co}^{2+}$  spins in GCO, the spins lying in the (111) planes, consist of Kagom e (KGM) spins separated by spins in the triangular (TRI) planes as first noted by Anderson [12]. In  $H = 0$  and  $T \ll T_N$ , spins in the neighboring KGM and TRI planes are antiparallel to each other but parallel within each plane. This provides

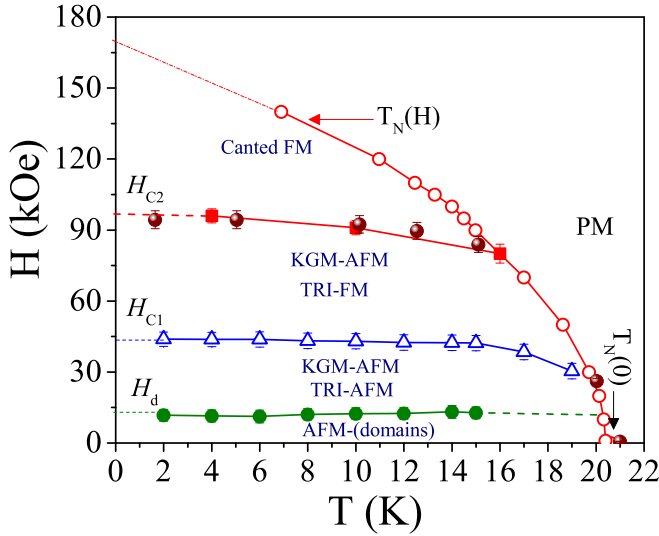


FIG. 9. The variation of the critical fields  $H_d$ ,  $H_{C1}$ , and  $H_{C2}$  with temperature ( $T$ ) obtained from the  $M$ - $H$  data. Data for  $H_{C1}$  and  $H_d$  is from the present work whereas the data for  $H_{C2}$  is from Refs. [13, 15]. The open circles represent the data for the magnetic field variation of  $T_N$  shown in Fig. 7 with the solid line marked  $T_N(H)$  representing the Eq.  $T_N(H) = T_N(0) - D_1 H^2$ . Other lines connecting the data points are drawn for visual clarity. See text for discussion of the nature of magnetic ordering in the different regions of  $H < H_d$ ,  $H_d < H < H_{C1}$ ,  $H_{C1} < H < H_{C2}$ , and  $H > H_{C2}$ .

overall AFM ordering although spins within each KGM and TRI planes are parallel to each other and lying in the (111) planes. Although direction of ordering within (111) planes is not uniquely defined, it is likely along either the  $[11\bar{2}]$  or  $[1\bar{1}0]$  directions, like that reported in cubic antiferromagnet MnO [48]. Since there are three equivalent such directions, this leads to formation of  $S$  domains. The weak transitions observed near  $H_d \sim 11$  kOe is due to elimination of these domains. Following Fabr eges *et al.* [24], the transition at  $H_{C1} \simeq 44$  kOe represents the alignment of the TRI magnetic moments along the applied  $H$  but the spins in the neighboring KGM planes are still antiparallel. Finally, at  $H = H_{C2} \simeq 97$  kOe, the spins in the KGM planes also flip to become nearly parallel to the applied  $H$ , applied along  $[11\bar{2}]$  directions, although some spins canting remains. This spin canting results in nonzero susceptibility and nonsaturation even at  $H = 550$  kOe. In summary, the transition at  $H_{C1}$  and  $H_{C2}$  are spin-flip transitions likely because the magnetic anisotropy in GCO is very large. Based on the above discussion, the  $H$ - $T$  phase diagram for GCO is represented in Fig. 9. The boundary separating the paramagnetic (PM) phase is based on Eq. (3) describing the variation of  $T_N$  with applied  $H$ .

## V. OPTICAL PROPERTIES

In this section we report our studies on the optical properties of GCO, which have not been reported in the literature till now. These measurements were performed using the diffuse reflectance spectroscopy in the UV visible and near IR range. In addition, we interpret our experimental results with our theoretically calculated density of states and

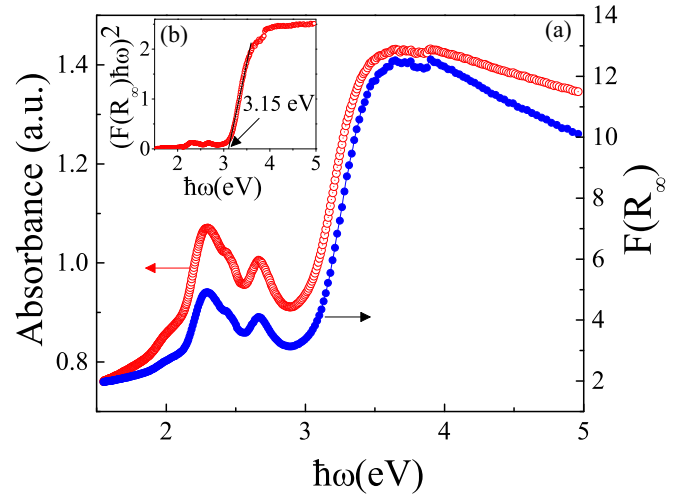


FIG. 10. (a) The variation of optical absorbance versus photon energy ( $\hbar\omega$ ) (shown on left-hand side scale) and Kubelka-Munk (K-M) function versus  $\hbar\omega$  (shown on right-hand side scale) for GCO; (b) The inset plot shows  $[F(R_\infty)\hbar\omega]^2$  versus  $\hbar\omega$ . The dotted line represents extrapolation of the linear region of the curve providing the optical energy band gap,  $E_g$ .

the band-structure using density functional theory DFT+ $U$  ( $U$  being the Columbic potential). We have employed the density functional theory (DFT) based calculations [49,50] using the projector augmented-wave (PAW) method [51,52] as implemented in Vienna *ab initio* simulation package (VASP) [53–55]. Perdew-Burke-Ernzerhof (PBE) parameterized generalized gradient approximation (GGA) for exchange correlation functional was employed [56]. The simulations were performed using 650 eV as the kinetic energy cut off of plane wave basis and Monkhorst-Pack of  $8 \times 8 \times 8$  k-grid mesh. The calculations are carried out using 14 atoms (2 formula units of the spinel primitive cell). The effects of electron localization were addressed by the approach of Dudarev *et al.* [57]. The Hund's coupling parameter,  $J$  is considered to be 0 eV and the Coulomb parameter  $U$  is considered to be 2 eV for Co and 0 eV for Ge. The electronic self-consistency is continued until the energy convergence is of the order of  $10^{-7}$  eV. Structural relaxations are performed until residual forces on each atom converge to less than  $10^{-4}$  eV/ .

To determine the optical band gap  $E_g$  from the Kubelka-Munk (KM) analysis of the experimental data [58,59], we employed KM equation  $[F(R_\infty)\hbar\omega]^2 = \alpha(\hbar\omega - E_g)$ , where  $R_\infty$  is the ratio of the reflectance of the sample and  $F(R_\infty)$  is the KM function [58]. In the above equation,  $\hbar\omega$  is the energy of the single photon and  $\alpha$  is absorption coefficient. The left-hand scale of Fig. 10(a) shows the intensity of optical absorbance of GCO versus the photon energy ( $\hbar\omega$ ) (eV) and the variation of  $F(R_\infty)$  as a function of photon energy is shown in the right-hand scale of Fig. 10(b). To determine the band gap, the function  $[F(R_\infty)\hbar\omega]^2$  versus  $\hbar\omega$  is plotted and the extrapolation of the band tail (as shown by the dotted lines) intercepts the photon energy axis at  $\hbar\omega = 3.156$  eV, which corresponds to the direct band gap of the system and is in good agreement with the theoretical calculations  $E_g \sim 3.28$  eV. Two additional subbands are observed at 2.29 and 2.66 eV



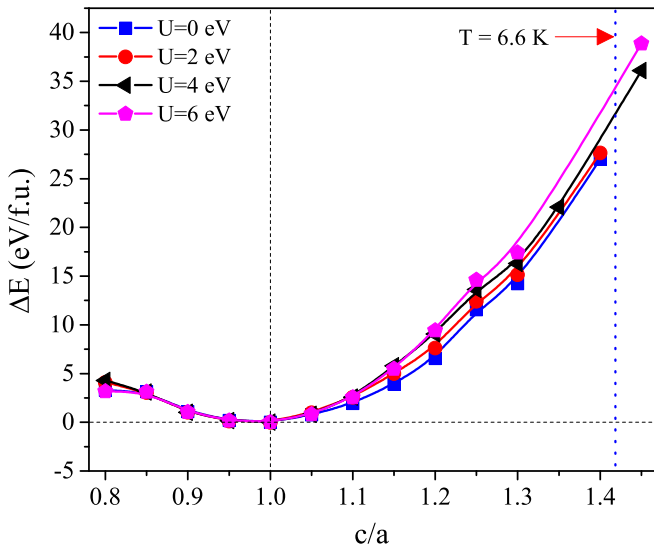


FIG. 11. The variation of total free energy as a function of tetragonal distortion ( $c/a$ ) for GCO for different values of  $U$ .

(Fig. 10) below the main absorption band (3.63 eV), which may be associated to the charge transition between  $\text{Co}^{2+}(e_g^\uparrow) \rightarrow \text{Co}^{2+}(t_{2g}^\uparrow)$  and  $\text{Co}^{2+}(t_{2g}^\downarrow) \rightarrow \text{Co}^{2+}(e_g^\downarrow)$ , respectively. The main absorption peak arises due to charge transfer between O ( $2p$ )  $\rightarrow$   $\text{Co}^{2+}(e_g^\uparrow)$  [60].

As noted earlier, several publications have reported cubic to tetragonal distortion in GCO at low temperature ( $T < 16$  K) [15,17,22–25]. To take account of this we have performed the DFT calculations to compute the total energies per formula unit after distorting the cubic structure, i.e.,  $c$  is fixed at 8.32 Å and  $a$  is varied between 10.4 Å and 5.546 Å. In Fig. 11, the total energy is plotted as a function of  $c/a$  ratio for different values of  $U$  ( $= 0, 2, 4$ , and 6 eV). The experimental observation at  $T = 6.6$  K is shown by blue dotted line in the Fig. 11. The DFT results show the cubic structure is more stable than the tetragonal structure for all the values of  $U$ . Hence, we carried out all the electronic structure calculations considering the cubic structure of GCO. Generally, in the DFT calculations the coulomb interaction parameter  $U$  is used to take account of the valence electron interactions [61]. The free parameter  $U$  has been chosen in such a way to match the experimental observations. To investigate the effect of  $U$  on the electronic structure we performed a detailed computation of the density of states of GCO system by varying  $U$  between 0 and 6 eV. Figures 12(a)–12(c) show the density of states plots for  $U = 0, 2, 4$  eV, respectively. For all the cases we find that the spin-up and spin-down density of states are nearly equal and exhibiting an antiferromagnetic configuration which is consistent with our experimental observations. For  $U = 0$  eV [Fig. 12(a)], the Fermi level falls below the maximum of the valence band indicating metallic nature of GCO in contradiction to the experimental observations. However, for the finite  $U$  values the system displays semiconductor/insulating behavior and the energy band gap gradually increases while increasing the  $U$  values. Figure 12(b) shows the density of states of GCO calculated using  $U = 2.0$  eV for Co ions. Close examination

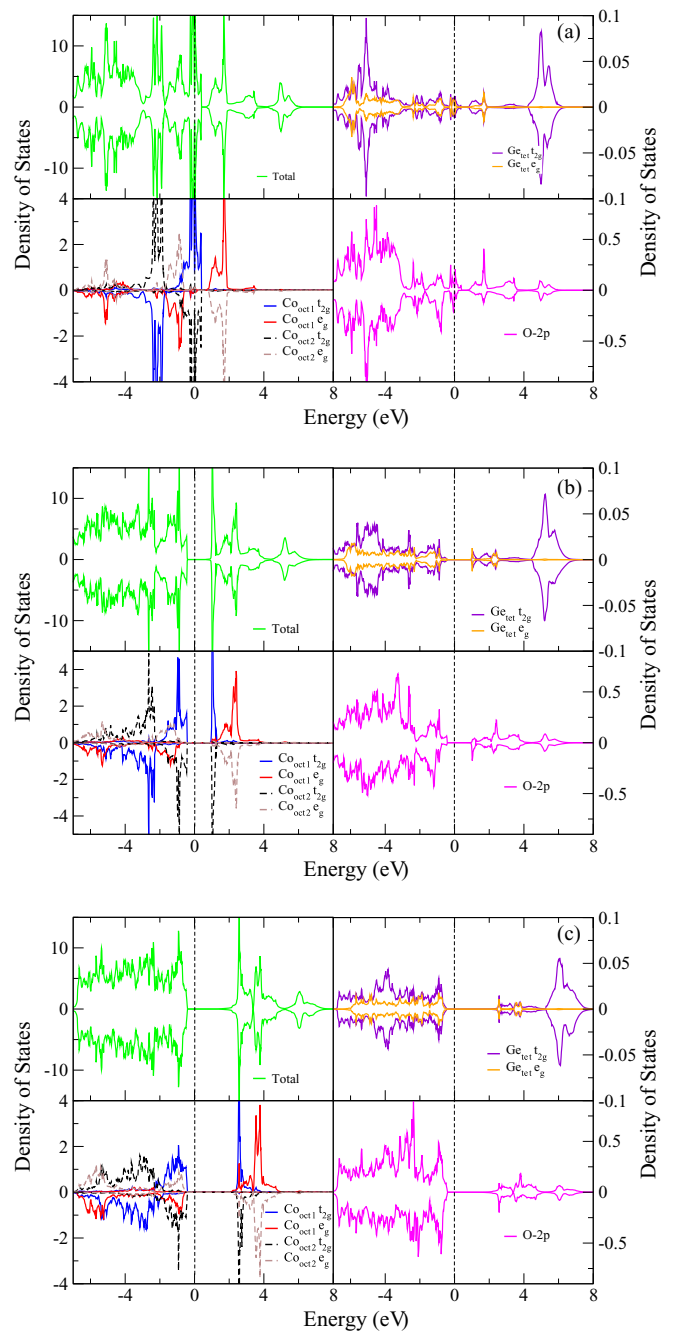


FIG. 12. Total and atom-projected electronic density of states of GCO is plotted as function of energy for (a)  $U = 0$  eV, (b)  $U = 2$  eV, and (c)  $U = 4$  eV for octahedral  $\text{Co}^{2+}$  ions.

of these plots reveals the electronic states at  $E \sim -1.39$  eV and  $-2.62$  eV pertaining to  $e_g^\uparrow$  and  $t_{2g}^\downarrow$ , respectively. However,  $t_{2g}^\uparrow$  states are localized at the top of the valence band maximum ( $\sim -0.88$  eV) and the conduction minimum ( $\sim 1.02$  eV). Interestingly, both the octahedral Co ions are willing to compensate each other contribution and yielding a stable antiferromagnetic structure of  $\text{GeCo}_2\text{O}_4$ . The contribution from tetrahedral  $\text{Ge}^{4+}$  is negligible to the total magnitude of density of states. All the optical transitions observed in GCO are listed in Table II together with those determined from the

TABLE II. The list of optical transitions and their positions obtained from the experimental results and DFT+ $U$ -based theoretical calculations.

| Transitions                                                                                           | $U$ (eV) | Type  | Theoretical energy (eV) | Experimental energy (eV) |
|-------------------------------------------------------------------------------------------------------|----------|-------|-------------------------|--------------------------|
| $\text{Co}^{2+}(t_{2g}^{\uparrow\downarrow}) \rightarrow \text{Co}^{2+}(t_{2g}^{\uparrow\downarrow})$ | 1.0      | $d-d$ | 1.14                    | 1.95                     |
|                                                                                                       | 2.0      |       | 1.96                    |                          |
|                                                                                                       | 3.0      |       | 2.72                    |                          |
|                                                                                                       | 4.0      |       | 3.49                    |                          |
| $\text{Co}^{2+}(e_g^{\uparrow}) \rightarrow \text{Co}^{2+}(t_{2g}^{\uparrow})$                        | 1.0      | $d-d$ | 1.76                    | 2.29                     |
|                                                                                                       | 2.0      |       | 2.25                    |                          |
|                                                                                                       | 3.0      |       | 2.72                    |                          |
|                                                                                                       | 4.0      |       | 3.49                    |                          |
| $\text{Co}^{2+}(e_g^{\downarrow}) \rightarrow \text{Co}^{2+}(t_{2g}^{\downarrow})$                    | 1.0      | $d-d$ | 1.95                    | 2.67                     |
|                                                                                                       | 2.0      |       | 2.38                    |                          |
|                                                                                                       | 3.0      |       | 2.79                    |                          |
|                                                                                                       | 4.0      |       | 3.89                    |                          |
| $\text{O}(2p) \rightarrow \text{Co}^{2+}(e_g^{\uparrow\downarrow})$                                   | 1.0      | $p-d$ | 2.45                    | 3.16                     |
|                                                                                                       | 2.0      |       | 3.26                    |                          |
|                                                                                                       | 3.0      |       | 3.89                    |                          |
|                                                                                                       | 4.0      |       | 4.48                    |                          |

DFT+ $U$  calculations and interpreted using the band structure and density of states of GCO (Figs. 12(a)–12(c) and 13). In what follows we discuss the changes occurring in the density of states as  $U$  is increased from  $U = 0$ –6 eV as shown in Figs. 12(a)–12(c). For  $U = 2$  eV, the  $t_{2g}^{\uparrow}$  states of octahedral  $\text{Co}^{2+}$  are localized both at the top of the valence band and bottom of the conduction band. However, for higher  $U$  values ( $\geq 4$  eV) the  $t_{2g}^{\uparrow}$  states in the conduction band dominates over the valence band. Similar features are noticeable in case of  $t_{2g}^{\downarrow}$  states. For the lower  $U$  values, the splitting in the  $t_{2g}^{\downarrow}$  states are visible in the valence band, which gradually diminishes and gets delocalized near the Fermi level for higher  $U$  values ( $\geq 4$  eV). Upon increasing  $U$  all the states ( $t_{2g}^{\uparrow\downarrow}$ ,  $e_g^{\uparrow\downarrow}$ ) move toward higher energies, where the shift in the  $e_g^{\downarrow}$  states are more significant as compared to the others.

To interpret the optical measurements, we use the density of states data to predict the possible optical transitions for dif-

ferent values of  $U$  ( $U = 1$ –4 eV), which are listed in Table II along with those values obtained from the experiments. We note that the theoretical values of the optical transitions for  $U = 2.0$  eV match quite well with the experimentally observed transitions, whereas the optical transitions corresponding to  $U \geq 3$  eV appeared to be higher than the experimental results. Moreover, the energy band gap of GCO calculated using the Coulombic interaction  $U = 2.0$  eV for Co-ions yields at  $\Gamma$ - $\Gamma$  and X-X points are 1.39 and 2.60 eV, respectively, whereas the indirect band gap at  $\Gamma$ -X occurs at 2.28 eV. It is noted that our calculations for  $U = 4.0$  eV (for the Co ions) give the direct X-X band gap of 3.28 eV (Fig. 13), which is in good agreement with our experimentally obtained optical band gap of 3.156 eV (Fig. 10).

## VI. SUMMARY AND CONCLUSIONS

The significant results presented here include the following: (i) The  $\chi_P$  versus  $T$  data above  $T_N$  and saturation magnetization below  $T_N$  in GCO have been interpreted using the same set of parameters for  $\text{Co}^{2+}$  ions, namely effective spin  $S = 1/2$  and  $g = 6.155$ ; (ii) these parameters also explain the measured magnetic moment =  $3.02 \mu_B$  per  $\text{Co}^{2+}$  reported by Diaz *et al.* using neutron diffraction; (iii) our analysis shows that neglecting the temperature independent term in magnetic susceptibility makes a significant difference on the determined parameters; (iv) fitting the magnetic susceptibility data to HTS, the magnitude of the dominant ferromagnetic exchange constant  $J_1/k_B = 14.7$  K has been determined; (v) the plot of  $\mu_{\text{eff}}/\mu_B$  in Fig. 4(b) shows the presence of short-range 2D ferromagnetic order near 100 K, in agreement with the broad peak in  $C_p/T$  versus  $T$  data of Lashley *et al.* [22]; (vi) Electronic states of  $\text{Ge}^{4+}$  and  $\text{Co}^{2+}$  in GCO are determined from the XPS studies and Rietveld refinement of the XRD patterns establishes  $\text{Ge}^{4+}$  and  $\text{Co}^{2+}$  occupying the tetrahedral and octahedral sites respectively; and (vii) a direct energy band gap  $E_g = 3.156$  eV in GCO is determined

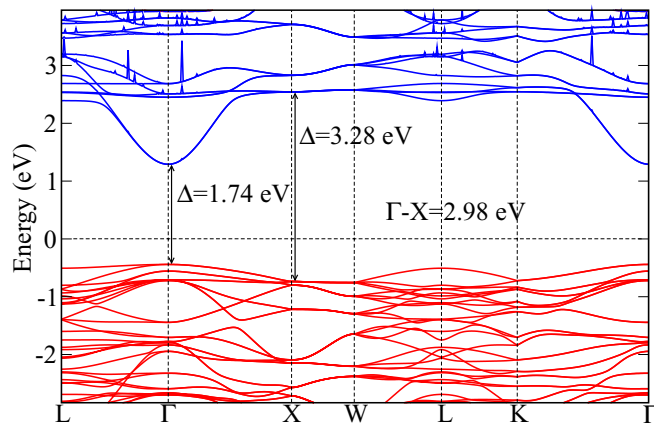


FIG. 13. The band structure of GCO is plotted with the symmetry points in the reciprocal lattice for  $U = 4.0$  eV for  $\text{Co}^{2+}$  ions.

from the diffuse reflectance spectroscopy which is in good agreement with those obtained from DFT+ $U$  calculations ( $E_g = 3.28$  eV). The remaining issues for complete understanding of the magnetic properties of GCO include the determination of the important interlayer AFM exchange constants, interpretation of the AFMR modes reported by Okubo *et al.* [27], and theoretical interpretation of the critical fields of Fig. 9 in terms of the anisotropy and exchange constants in a manner e.g. reported for the quasi-2D, spin 1/2 antiferromagnet copper formate tetrahydrate [62]. However, as noted earlier, GCO has two types of spins (KGM and TRI) and several different exchange couplings among them making this task quite challenging.

## ACKNOWLEDGMENTS

P.P. acknowledges the FIST program of Department of Science and Technology, India, for partial support of this work (Grants No. SR/FST/PSII-020/2009 and No. SR/FST/PSII-037/2016). P.P., S.G., and D.C.J. acknowledge the Central Instrument Facility (CIF) of the Indian Institute of Technology Guwahati for partial support of this work. A.S. would like to acknowledge Sheikh Saqr Laboratory (SSL) and International Centre for Materials Science (ICMS) at Jawaharlal Nehru Centre for Advanced Scientific Research (JNCASR) for various experimental facilities. We would like to acknowledge supercomputing facility, PARM-ISHAN, of IITG where some simulations were performed.

- 
- [1] G. Wang, X. Gao, and P. Shen, *J. Power Sources* **192**, 719 (2009).
- [2] S. Jin, G. Yang, H. Song, H. Cui, and C. Wang, *ACS Appl. Mater. Interfaces* **7**, 24932 (2015).
- [3] Y. Sharma, N. Sharma, G. Subba Rao, and B. Chowdari, *Adv. Funct. Mater.* **17**, 2855 (2007).
- [4] S. Yuvaraj, R. H. Vignesh, L. Vasylechko, Y. Lee, and R. K. Selvan, *RSC Adv.* **6**, 69016 (2016).
- [5] K. De Strooper, A. Govaert, C. Dauwe, and G. Robbrecht, *Phys. Status Solidi A* **37**, 127 (1976).
- [6] K. De Strooper, *Phys. Status Solidi A* **39**, 431 (1977).
- [7] J. Hubsch and G. Gavaille, *J. Magn. Magn. Mater.* **66**, 17 (1987).
- [8] S. Thota, M. Reehuis, A. Maljuk, A. Hoser, J.-U. Hoffmann, B. Weise, A. Waske, M. Krautz, D. C. Joshi, S. Nayak, S. Ghosh, P. Suresh, K. Dasari, S. Wurmehl, O. Prokhnenko, and B. Büchner, *Phys. Rev. B* **96**, 144104 (2017).
- [9] S. Thota, V. Narang, S. Nayak, S. Sambasivam, B. Choi, T. Sarkar, M. S. Andersson, R. Mathieu, and M. S. Seehra, *J. Phys.: Condens. Matter* **27**, 166001 (2015).
- [10] J. Srivastava, S. Ramakrishnan, V. Marathe, G. Chandra, R. Vijayaraghavan, J. Kulkarni, V. Darshane, and S. Singh, *J. Appl. Phys.* **61**, 3622 (1987).
- [11] E. Hermon, D. J. Simkin, R. J. Haddad, and W. B. Muir, *J. Phys. Colloques* **38**, C1-131 (1977).
- [12] P. W. Anderson, *Phys. Rev.* **102**, 1008 (1956).
- [13] S. Diaz, S. de Brion, M. Holzapfel, G. Chouteau, and P. Strobel, *Physica B (Amsterdam)* **346**, 146 (2004).
- [14] S. Diaz, S. de Brion, G. Chouteau, B. Canals, V. Simonet, and P. Strobel, *Phys. Rev. B* **74**, 092404 (2006).
- [15] T. Hoshi, H. A. Katori, M. Kosaka, and H. Takagi, *J. Magn. Magn. Mater.* **310**, e448 (2007).
- [16] M. Matsuda, T. Hoshi, H. Aruga Katori, M. Kosaka, and H. Takagi, *J. Phys. Soc. Jpn.* **80**, 034708 (2011).
- [17] T. Watanabe, S. Hara, and S.-I. Ikeda, *Phys. Rev. B* **78**, 094420 (2008).
- [18] M. S. Seehra, V. Singh, and S. Thota, *J. Appl. Phys.* **110**, 113907 (2011).
- [19] M. S. Seehra, V. Singh, S. Thota, B. Prasad, and J. Kumar, *Appl. Phys. Lett.* **97**, 112507 (2010).
- [20] W. Schiessl, W. Potzel, H. Karzel, M. Steiner, G. M. Kalvius, A. Martin, M. K. Krause, I. Halevy, J. Gal, W. Schäfer, G. Will, M. Hillberg, and R. Wäppling, *Phys. Rev. B* **53**, 9143 (1996).
- [21] Y. Horibe, M. Shingu, K. Kurushima, H. Ishibashi, N. Ikeda, K. Kato, Y. Motome, N. Furukawa, S. Mori, and T. Katsufuji, *Phys. Rev. Lett.* **96**, 086406 (2006).
- [22] J. C. Lashley, R. Stevens, M. K. Crawford, J. Boerio-Goates, B. F. Woodfield, Y. Qiu, J. W. Lynn, P. A. Goddard, and R. A. Fisher, *Phys. Rev. B* **78**, 104406 (2008).
- [23] P. T. Barton, M. C. Kemei, M. W. Gaultois, S. L. Moffitt, L. E. Darago, R. Seshadri, M. R. Suchomel, and B. C. Melot, *Phys. Rev. B* **90**, 064105 (2014).
- [24] X. Fabrèges, E. Ressouche, F. Duc, S. de Brion, M. Amara, C. Detlefs, L. Paolasini, E. Suard, L.-P. Regnault, B. Canals, P. Strobel, and V. Simonet, *Phys. Rev. B* **95**, 014428 (2017).
- [25] K. Tomiyasu, A. Tominaga, S. Hara, H. Sato, T. Watanabe, S.-I. Ikeda, H. Hiraka, K. Iwasa, and K. Yamada, in *J. Phys. Conf. Ser.*, Vol. 320 (IOP Publishing, Bristol, UK, 2011), p. 012038.
- [26] K. Tomiyasu, M. K. Crawford, D. T. Adroja, P. Manuel, A. Tominaga, S. Hara, H. Sato, T. Watanabe, S. I. Ikeda, J. W. Lynn, K. Iwasa, and K. Yamada, *Phys. Rev. B* **84**, 054405 (2011).
- [27] S. Okubo, H. Ohta, T. Ijima, T. Yamasaki, W. Zhang, S. Hara, S. Ikeda, H. Oshima, M. Takahashi, K. Tomiyasu *et al.*, *Z. Phys. Chem.* **231**, 827 (2017).
- [28] M. E. Lines, *Phys. Rev.* **131**, 546 (1963).
- [29] Z. Wang and M. S. Seehra, *J. Phys.: Condens. Matter* **29**, 225803 (2017).
- [30] N. McIntyre and D. Zetaruk, *Anal. Chem.* **49**, 1521 (1977).
- [31] T.-H. Ko, K. Devarayan, M.-K. Seo, H.-Y. Kim, and B.-S. Kim, *Sci. Rep.* **6**, 20313 (2016).
- [32] H. Nesbitt and D. Banerjee, *Am. Mineral.* **83**, 305 (1998).
- [33] M. Oku and K. Hirokawa, *J. Electron Spectrosc. Relat. Phenom.* **8**, 475 (1976).
- [34] P. Pramanik, S. Thota, S. Singh, D. C. Joshi, B. Weise, A. Waske, and M. S. Seehra, *J. Phys.: Condens. Matter* **29**, 425803 (2017).
- [35] W. E. Morgan and J. R. Van Wazer, *J. Phys. Chem.* **77**, 964 (1973).
- [36] R. Gopalakrishnan, B. Chowdari, and K. Tan, *Solid State Ion.* **51**, 203 (1992).
- [37] L. Jiang, A. G. Fitzgerald, M. J. Rose, K. Christova, and V. Pamukchieva, *J. Non-Cryst. Solids* **297**, 13 (2002).
- [38] S. Kai Wang, H.-G. Liu, and A. Toriumi, *Appl. Phys. Lett.* **101**, 061907 (2012).

- [39] K. Prabhakaran and T. Ogino, *Surf. Sci.* **325**, 263 (1995).
- [40] S. Thota and S. Singh, in *Magnetic Spinel—Synthesis, Properties and Applications*, edited by M. S. Seehra (IntechOpen, Rijeka, 2017), Chap. 4.
- [41] P. Burgardt and M. S. Seehra, *Solid State Commun.* **22**, 153 (1977).
- [42] H.-J. Schmidt, A. Lohmann, and J. Richter, *Phys. Rev. B* **84**, 104443 (2011).
- [43] J. D. Rall and M. S. Seehra, *J. Phys.: Condens. Matter* **24**, 076002 (2012).
- [44] J. W. Orton, *Electron Paramagnetic Resonance: An Introduction to Transition Group Ions in Crystals* (Ilfie, Cambridge, UK, 1968).
- [45] M. E. Fisher, *Philos. Mag.* **7**, 1731 (1962).
- [46] V. Narang, D. Korakakis, and M. S. Seehra, *J. Magn. Magn. Mater.* **368**, 353 (2014).
- [47] Y. Shapira and S. Foner, *Phys. Rev. B* **1**, 3083 (1970).
- [48] M. S. Jagadeesh and M. S. Seehra, *Phys. Rev. B* **23**, 1185 (1981).
- [49] P. Hohenberg and W. Kohn, *Phys. Rev.* **136**, B864 (1964).
- [50] W. Kohn and L. J. Sham, *Phys. Rev.* **140**, A1133 (1965).
- [51] P. E. Blöchl, *Phys. Rev. B* **50**, 17953 (1994).
- [52] G. Kresse and D. Joubert, *Phys. Rev. B* **59**, 1758 (1999).
- [53] G. Kresse and J. Furthmüller, *Phys. Rev. B* **54**, 11169 (1996).
- [54] G. Kresse and J. Furthmüller, *Comput. Mater. Sci.* **6**, 15 (1996).
- [55] G. Kresse and J. Hafner, *Phys. Rev. B* **47**, 558 (1993).
- [56] J. P. Perdew, K. Burke, and M. Ernzerhof, *Phys. Rev. Lett.* **77**, 3865 (1996).
- [57] S. L. Dudarev, G. A. Botton, S. Y. Savrasov, C. J. Humphreys, and A. P. Sutton, *Phys. Rev. B* **57**, 1505 (1998).
- [58] P. Kubelka and F. Munk, *Z. Tech. Phys.* **12**, 593 (1931).
- [59] P. Kubelka, *J. Opt. Soc. Am.* **38**, 448 (1948).
- [60] S. Thota, A. Kumar, and J. Kumar, *Mater. Sci. Eng. B* **164**, 30 (2009).
- [61] S. Ghosh, S. Singh, D. C. Joshi, P. Pramanik, S. Ghosh, P. K. Mishra, and S. Thota, *Phys. Rev. B* **98**, 235119 (2018).
- [62] M. S. Seehra and T. G. Castner, Jr., *Phys. Rev. B* **1**, 2289 (1970).